Supporting Information

for

Observation-Based Assessment of Contrail Climate Effects across the Euro-Atlantic Region in 2023

Irene Ortiz*[1], Ermioni Dimitropoulou[2], Pierre de Buyl[2], Nicolas Clerbaux[2], Jeroen van Gent[3], Hugues Brenot[3], Javier García-Heras[1], and Manuel Soler[1]

[1]Department of Aerospace Engineering, University Carlos III of Madrid, Avenida de la Universidad 30, 28911 Madrid, Spain
[2]Royal Meteorological Institute of Belgium, 3 Avenue Circulaire, 1180 Brussels, Belgium
[3]Royal Belgian Institute for Space Aeronomy, 3 Avenue Circulaire, 1180 Brussels, Belgium

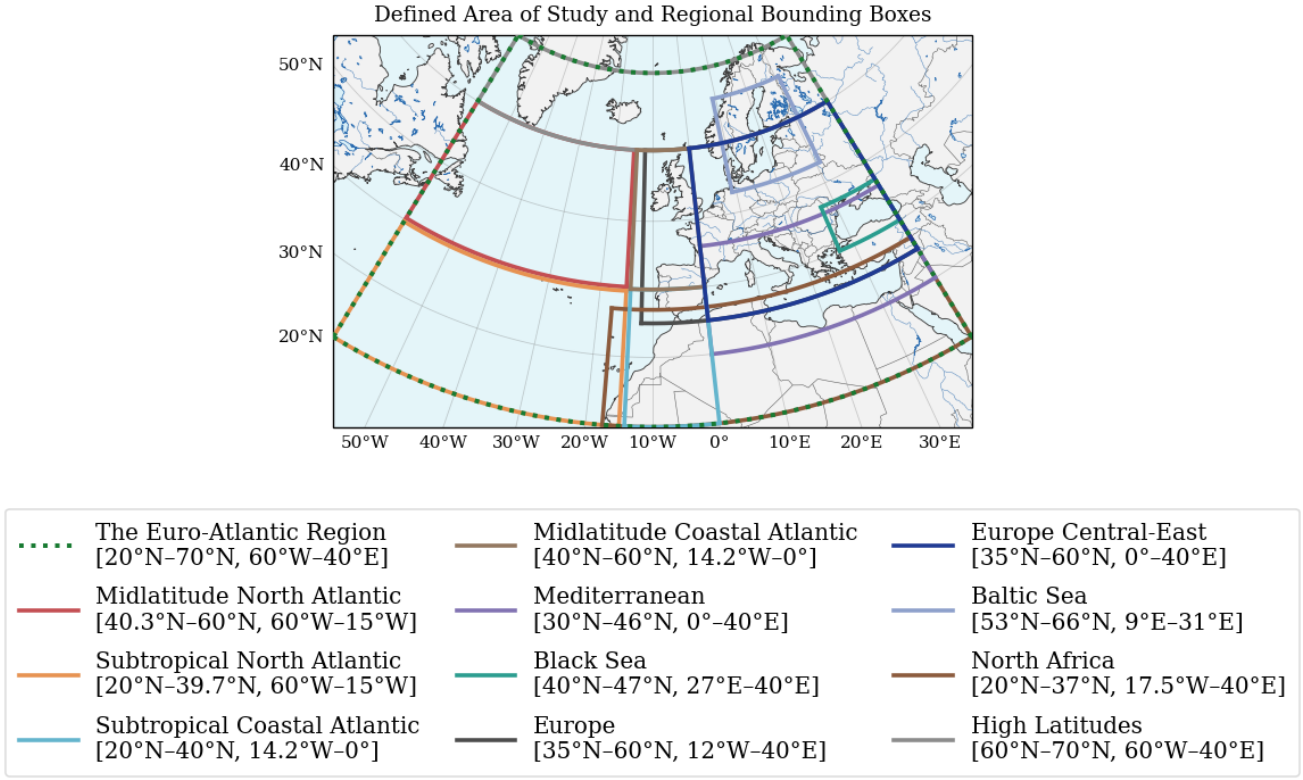

Figure 1: The study domain is divided into regional bounding boxes covering the North Atlantic, Europe, North Africa, and adjacent coastal and high-latitude areas. Yearly contrail coverage and aircraft activity are analyzed separately within each region to account for spatial differences in meteorological conditions and air traffic density that influence persistent contrail formation.

*Email: irortiza@ing.uc3m.es

Region	Aircraft crossings (%)	RF_+ (%)	Contrail contribution (%)	Coverage (%)	Density (km km^{-2})	Area/dist. (m^2 m^{-1})	Area/hr (km^2 h^{-1})	Area/flight (km^2 flight^{-1})
The entire Euro-Atlantic Region	100.00	100.00	100.00	0.18	0.13	21.40	14.59	17.82
Europe	77.16	29.84	36.59	0.21	0.42	7.37	4.71	5.86
Europe Central-East	69.41	11.93	14.67	0.12	0.43	5.09	3.41	3.22
Coastal Atlantic	34.08	24.50	38.77	0.38	0.19	30.44	19.75	16.39
Coastal Atlantic (Midlatitudes)	30.93	16.58	19.07	0.48	0.33	20.49	12.66	10.74
Coastal Atlantic (Subtropical)	12.19	7.92	19.70	0.30	0.09	63.15	46.11	21.96
North Atlantic	6.24	59.11	37.08	0.26	0.04	488.17	431.01	98.89
North Atlantic (Midlatitudes)	4.09	26.85	13.14	0.23	0.08	167.67	72.91	46.37
North Atlantic (Subtropical)	3.09	30.85	23.18	0.27	0.01	705.33	642.35	243.50
Mediterranean	60.20	7.91	10.85	0.12	0.32	9.04	6.97	3.57
Baltic Sea	13.46	1.29	1.74	0.08	0.14	8.29	4.83	3.65
Black Sea	9.79	0.53	0.27	0.04	0.35	1.59	0.71	0.66
North Africa	39.56	9.07	25.14	0.11	0.04	72.56	51.93	17.45
High Latitudes	6.15	0.86	0.84	0.01	0.03	5.44	3.67	3.33

Table 1: Regional statistics of aviation activity and contrail occurrence across the study domain. The first three columns show the relative contributions of each region to total aircraft crossings, positive contrail radiative forcing (RF_+), and contrail-covered area, expressed as percentages of the full study domain (The Euro-Atlantic region). The remaining columns report mean contrail occurrence metrics derived from satellite observations and air traffic data. Contrail coverage represents the mean fractional regional area covered by satellite-detected contrails (%). Air traffic density is defined as total flown distance normalized by grid-cell area (km km^{-2}). Normalized contrail metrics include contrail-covered area per flown distance (m^2 m^{-1}), per aircraft hour (km^2 h^{-1}), and per flight (km^2 flight^{-1}). For distance-based normalization, only flights within the preceding 5 h and above 8 km altitude are considered to isolate aircraft with the potential to generate the observed contrails. The normalized metrics indicate generally low contrail occurrence relative to air traffic activity across continental Europe, high latitudes, and most oceanic regions. In contrast, a pronounced maximum is observed over the North Atlantic, particularly at lower latitudes (here referred to as the subtropical region), where the detection rate relative to aircraft crossings is highest.

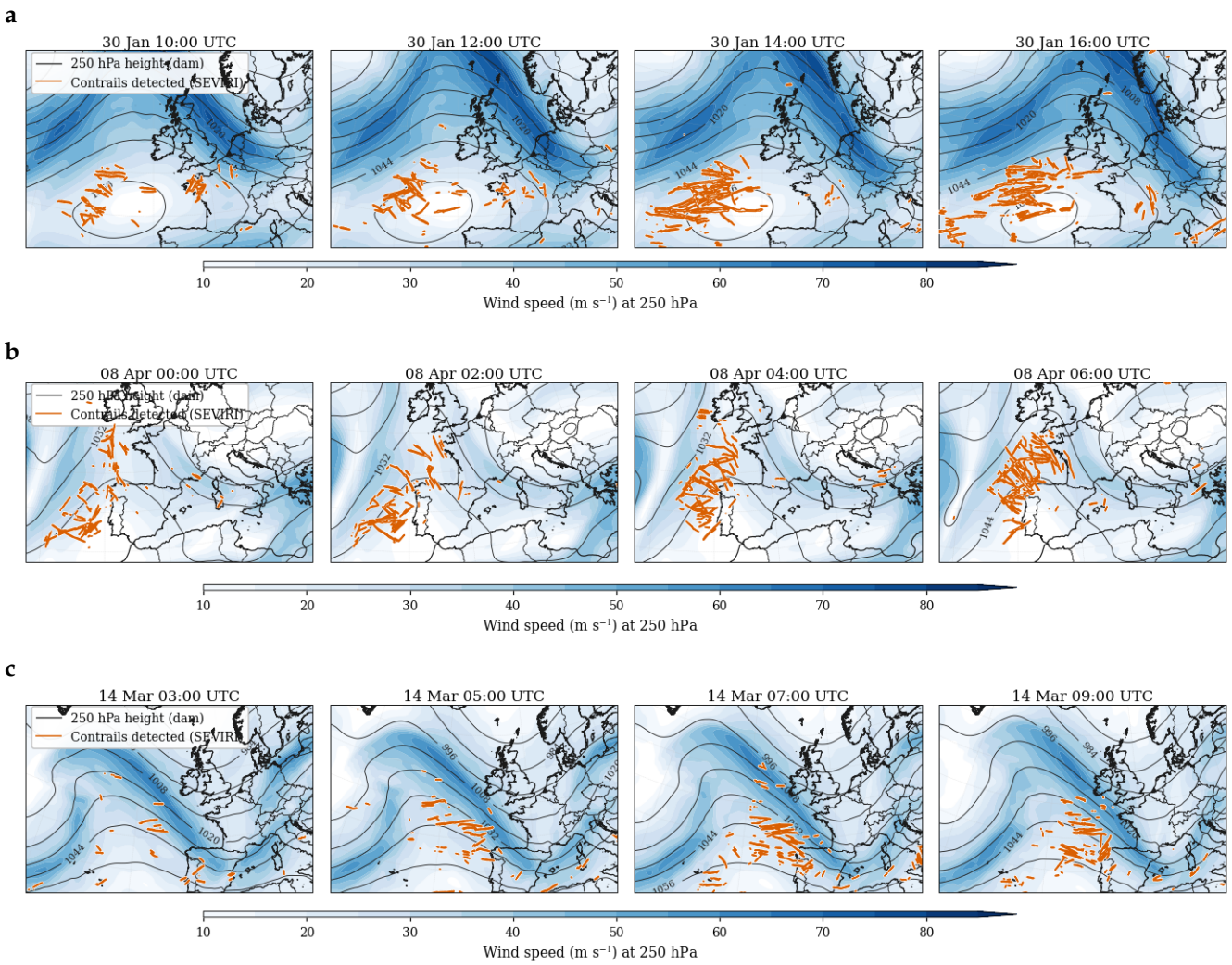

Figure 2: Examples of contrail outbreak evolution in relation to the upper-level jet stream for three separate cases: (a) 14 March 2023, (b) 8 April 2023, and (c) 30 January 2023. Each row shows a time sequence (UTC) of ERA5 250-hPa wind speed (shading) and geopotential height (contours), with detected contrails overlaid in orange. A well-defined upper-level jet is present in all cases, with peak wind speeds reaching $\sim$ 60–70ms^{-1} in cases (a) and (c), and lower values in case (b). Contrails are consistently sparse within the jet core and do not develop into outbreaks there; instead, they cluster along the southern flank of the jet and in regions of strong wind speed gradients, remaining displaced from areas of maximum wind speed. This recurring spatial relationship suggests that contrail persistence are favored in jet-adjacent regions characterized by higher upper-tropospheric humidity and relatively weaker winds. As the flow advects eastward, these contrails are typically transported toward adjacent coastal regions. Given the bounding box definition (Fig. 1), many contrails detected over coastal regions formed earlier over the open North Atlantic; their warming impact should therefore be attributed to transatlantic aviation.

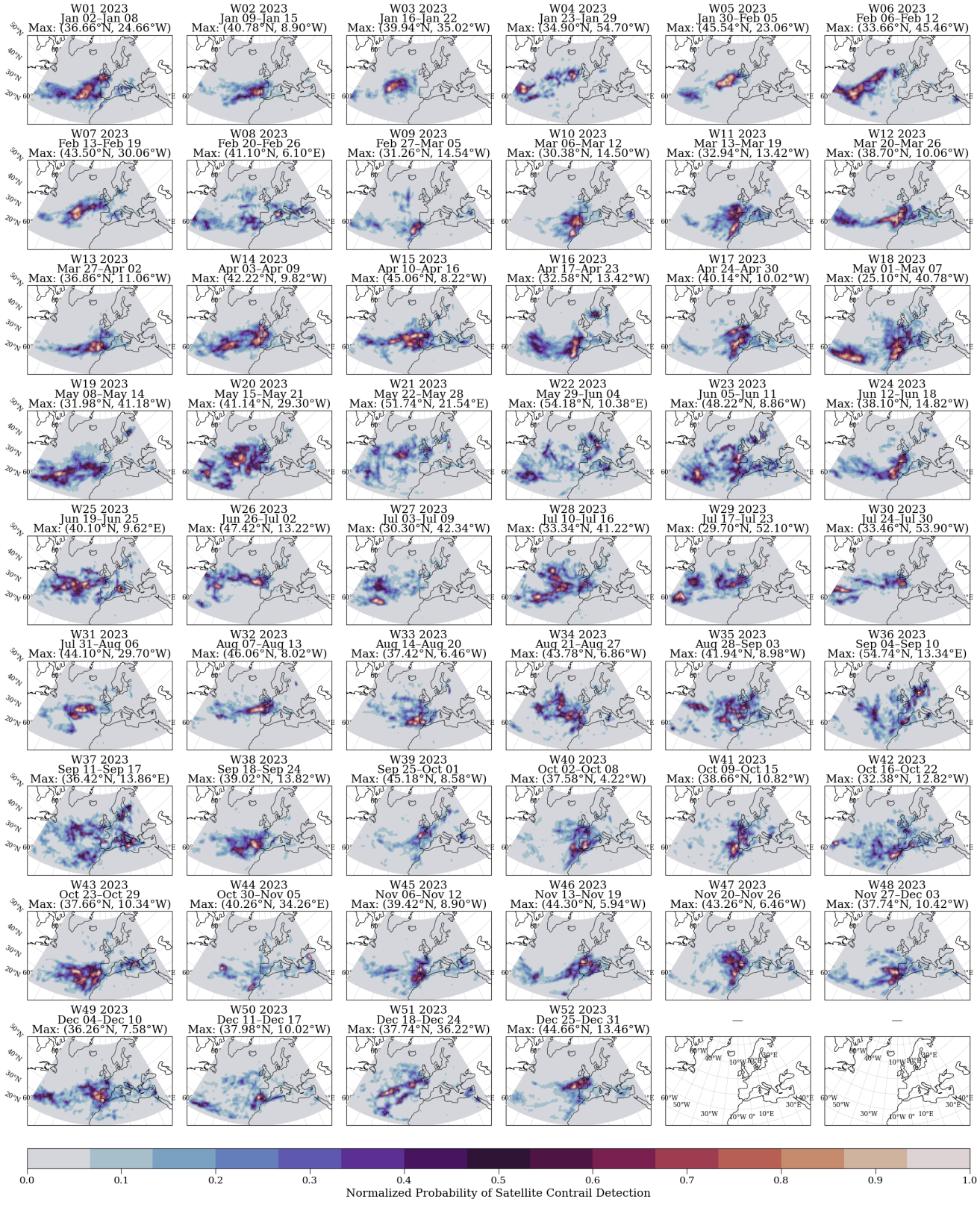

Figure 3: Geographical distribution of the probability of contrail detection over the Euro-Atlantic region (60°W–40°E, 20°N–70°N), averaged by ISO weeks (International Organization for Standardization calendar weeks), covering all 52 weeks of 2023. These results complement the monthly maps presented in the main document by providing enhanced temporal continuity. They reveal that contrail occurrence is concentrated in relatively localized spatial regions that systematically shift from week to week. This clear displacement highlights the strong dependence of contrail formation and persistence on day-to-day meteorological conditions, which is not captured by coarser temporal averaging.

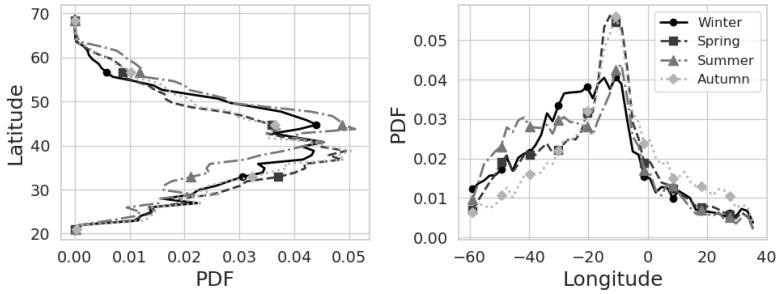

Figure 4: Seasonal probability density functions (PDFs) of detected contrail coverage across latitude and longitude within the study domain for 2023. Although seasonal averaging smooths much of the spatial structure, the distributions show a modest northward shift in summer, following the seasonal migration of the jet stream. In autumn, an eastward displacement is evident, indicating reduced contrail occurrence over the North Atlantic and increased occurrence over continental Europe.

Route	**%**
EU–EU	62.83
AS–EU	14.78
AF–EU	8.21
NA–EU	6.32
AS–AS	3.75
AS–NA	2.04
SA–EU	0.76

Route	**%**
AF–AF	0.58
AF–AS	0.51
AF–NA	0.10
AS–SA	0.07
EU–AUS	0.05
AF–SA	0.01

Table 2: Average daily distribution of flight connections within the study area, classified by origin–destination pairs using short codes: EU (Europe), AS (Asia), AF (Africa), NA (North America), SA (South America), and AUS (Australia). The data shows that intra-European flights dominate the traffic ($\sim$ 63%), followed by connections with Africa, Asia, and North America, while all other routes together account for less than 8% of aircraft present in the region at any given time. Notably, Asian routes represent more than 20% of the traffic.

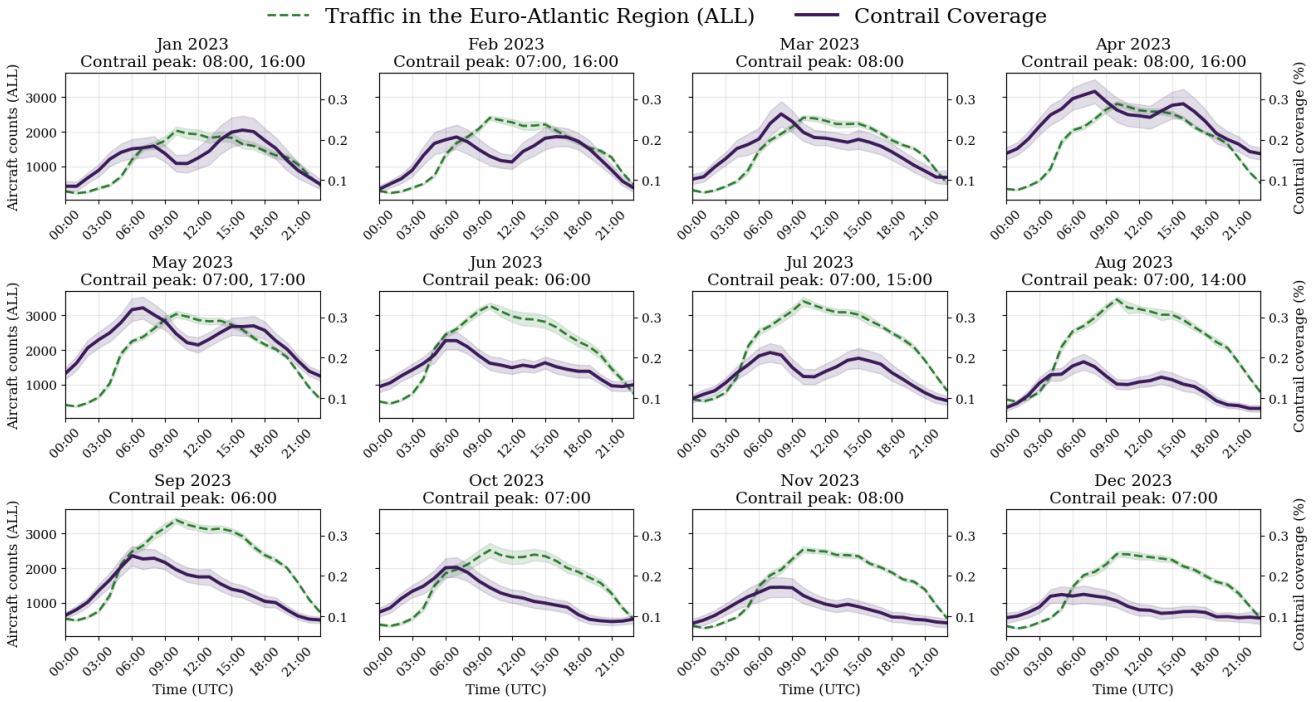

Figure 5: Diurnal cycle of contrail coverage by month in 2023, shown alongside aircraft counts. Contrail coverage (solid line) is compared with traffic along the Euro-Atlantic region (green dashed). Across all seasons, a pronounced morning maximum in contrail coverage occurs between 06:00–08:00 UTC, with a secondary afternoon peak between approximately 14:00–17:00 UTC. These maxima do not coincide with peaks in flight activity over the study region, which typically occur around 10:00–11:00 UTC. Instead, the timing of the contrail peaks aligns more closely with the diurnal cycle of transatlantic flights, a small subset of the total air traffic over the study region (see Fig. 3 in the main document), suggesting that long-haul oceanic routes play a key role in driving the observed diurnal patterns.

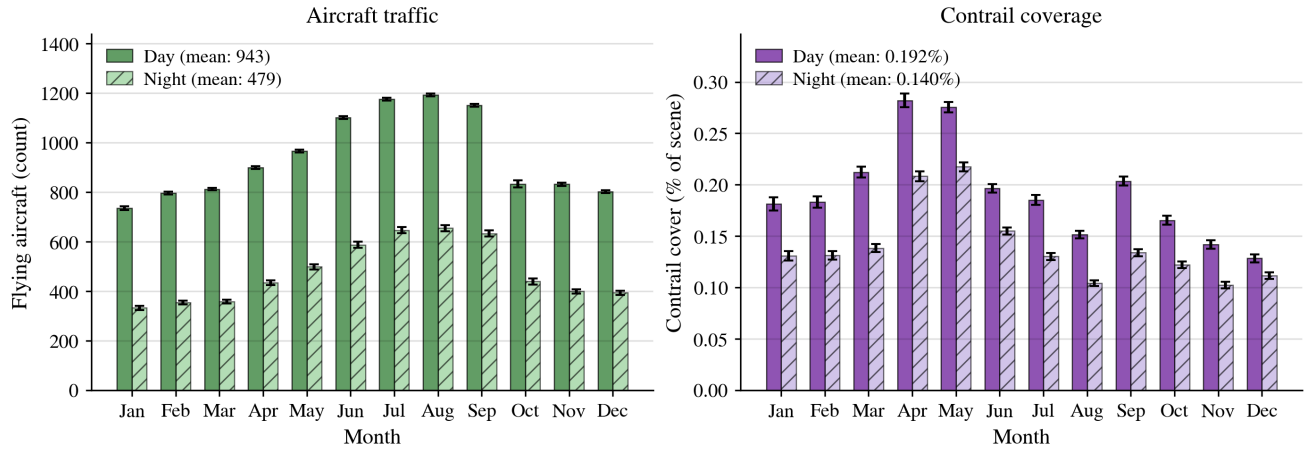

Figure 6: Monthly variability in spatial coverage and in the number of aircraft aloft at the time of each snapshot within the considered domain, with results separated by daytime and nighttime conditions. The results show a clear difference between the number of aircraft aloft during day and night, which is consistently reflected in the contrail coverage, with a significant decrease in detected coverage from daytime to nighttime throughout the year. In contrast, the monthly evolution of contrail coverage does not directly follow the aircraft traffic trend. Although summer represents the busiest period for aviation, it corresponds to one of the seasons with the lowest detected contrail coverage. Instead, contrail coverage peaks in April and May, indicating that the seasonal variability in detected coverage is primarily driven by meteorological conditions controlling contrail persistence and observability, rather than by variations in air traffic activity alone.

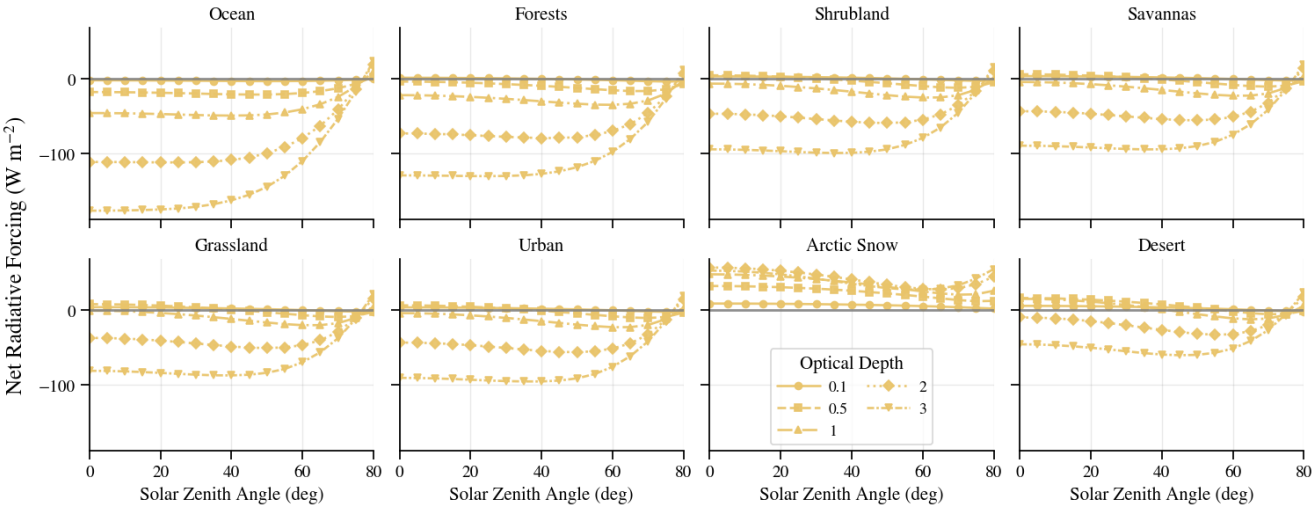

Figure 7: Balance between shortwave and longwave radiative forcing as a function of solar zenith angle (0°–80°) under daylight conditions. Curves show median net radiative forcing across cloud effective radius, cloud-top height, and surface albedo for contrail-representative cloud optical depths (0–3), separated by land-cover class. Over the ocean, net radiative forcing remains negative for all optical depths at solar zenith angles $< 75°$, indicating dominant shortwave cooling. Over land, similar cooling occurs below 75° for most surface types, except at low optical depths (< 0.5–1) where some warming contrails can be found under sunlit conditions. In contrast, Arctic snow exhibits positive net radiative forcing across all optical depths and solar zenith angles, highlighting the suppression of shortwave cooling over high-albedo surfaces; however, this regime is underrepresented in the results.

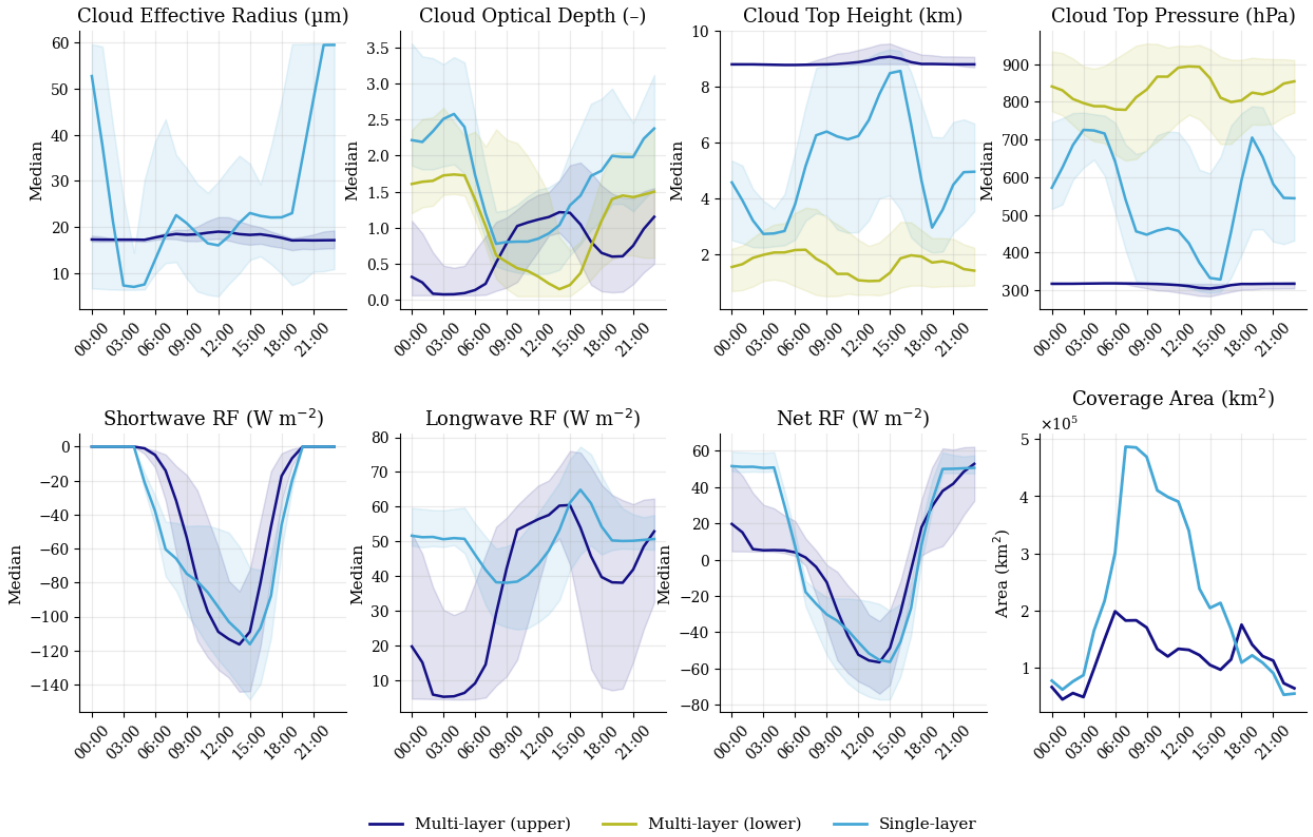

Figure 8: Temporal evolution of contrail properties and radiative forcing for the outbreak on 8 April 2023 throught the entire day (Fig. 2c).Hourly averaged contrail cloud properties and their corresponding radiative forcing are presented for contrail pixels identified using a neural network. The curves represent mean values, while the shaded areas indicate interquartile ranges. The results are separated into multilayer and single-layer (clear-sky) conditions. Single-layer contrails more frequently exhibit physically unrealistic retrievals, including anomalously low cloud-top heights and elevated optical depths, particularly during periods of low coverage when sampling uncertainty is highest. The impact of these biases on radiative forcing cannot be directly inferred from comparison with multilayer cases, as cloud–cloud interactions tend to modify the net forcing differently in each case. The sensitivity analysis in the main text addresses this by recalculating radiative forcing after constraining unrealistically high optical depth values, which is the most influential cloud parameter on radiative forcing estimates. Cloud-top heights below 6 km were automatically set to 6 km in all main-document calculations to comply with the minimum value required by the lookup tables.

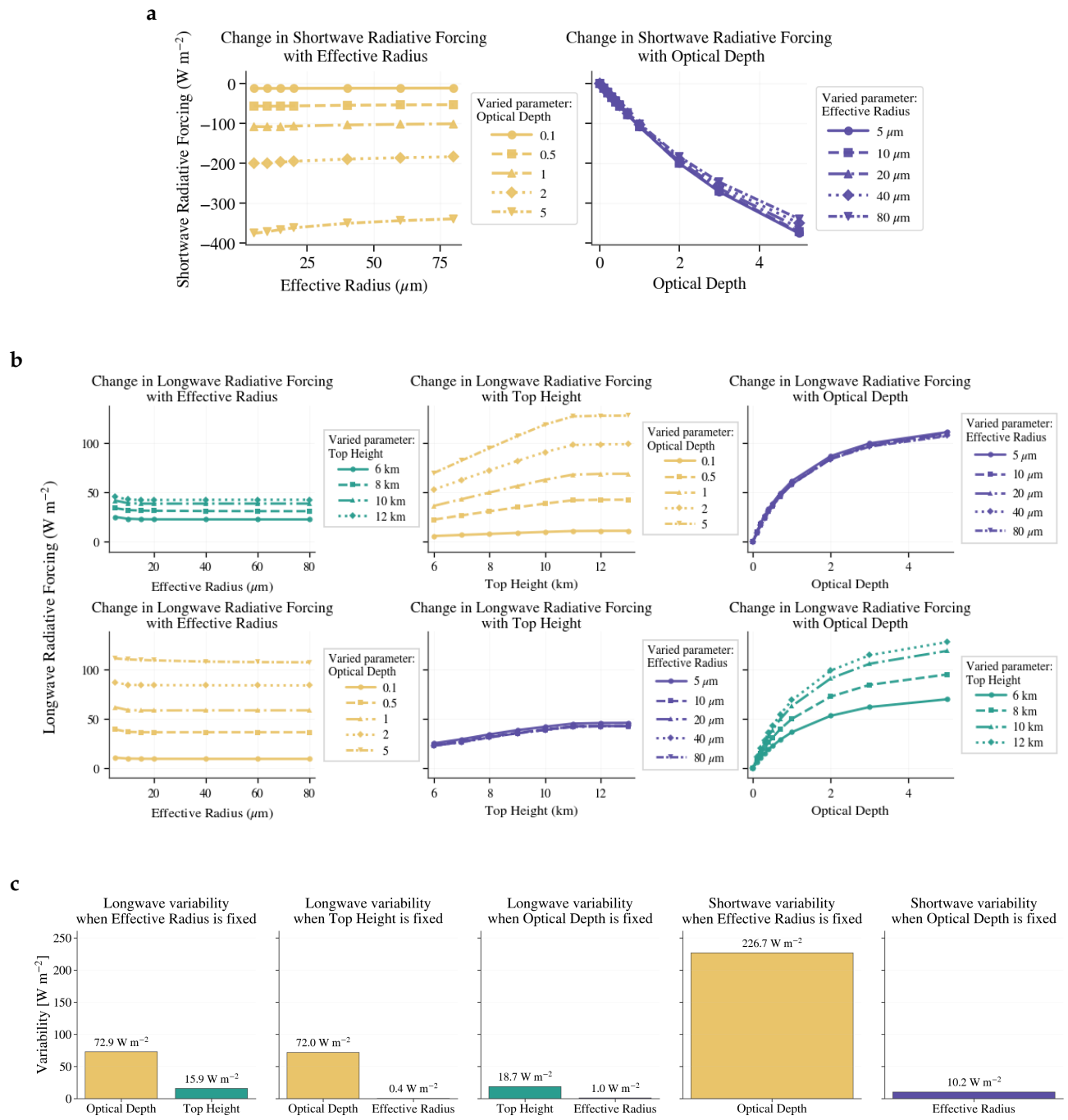

Figure 9: Sensitivity of simulated contrail radiative forcing derived from look-up tables to key cloud properties. Panels (a) and (b) show results for contrails over the ocean, with cloud optical depth values ranging from 0 to 5, while panel (c) shows results for the full optical depth range, up to 30. In shortwave radiative forcing (a), cloud optical depth produces large changes of roughly 200–400 W m^{-2} across the full range and about 250 W m^{-2} within the contrail-relevant range (optical depth $\approx$ 0.05–2.5), while effective radius has only a small influence (generally less than about 15 W m^{-2}). In longwave radiative forcing (b), cloud optical depth produces changes of about 50–120 Wm^{-2}, cloud-top height contributes about 20–40 Wm^{-2}, and effective radius remains small (typically below about 10–15 Wm^{-2}). Panel (c) summarizes the variability using interquartile ranges calculated from the look-up tables for entire optical depth range represented in the look-up tables. This analysis confirms that cloud optical depth is the dominant driver of variability in radiative forcing. Overestimation of optical depth may introduce a negative bias per pixel of up to 227 W m^{-2} in shortwave radiation and a positive bias of up to 72 W m^{-2} in longwave radiation, far exceeding the contributions from effective radius and cloud-top height.

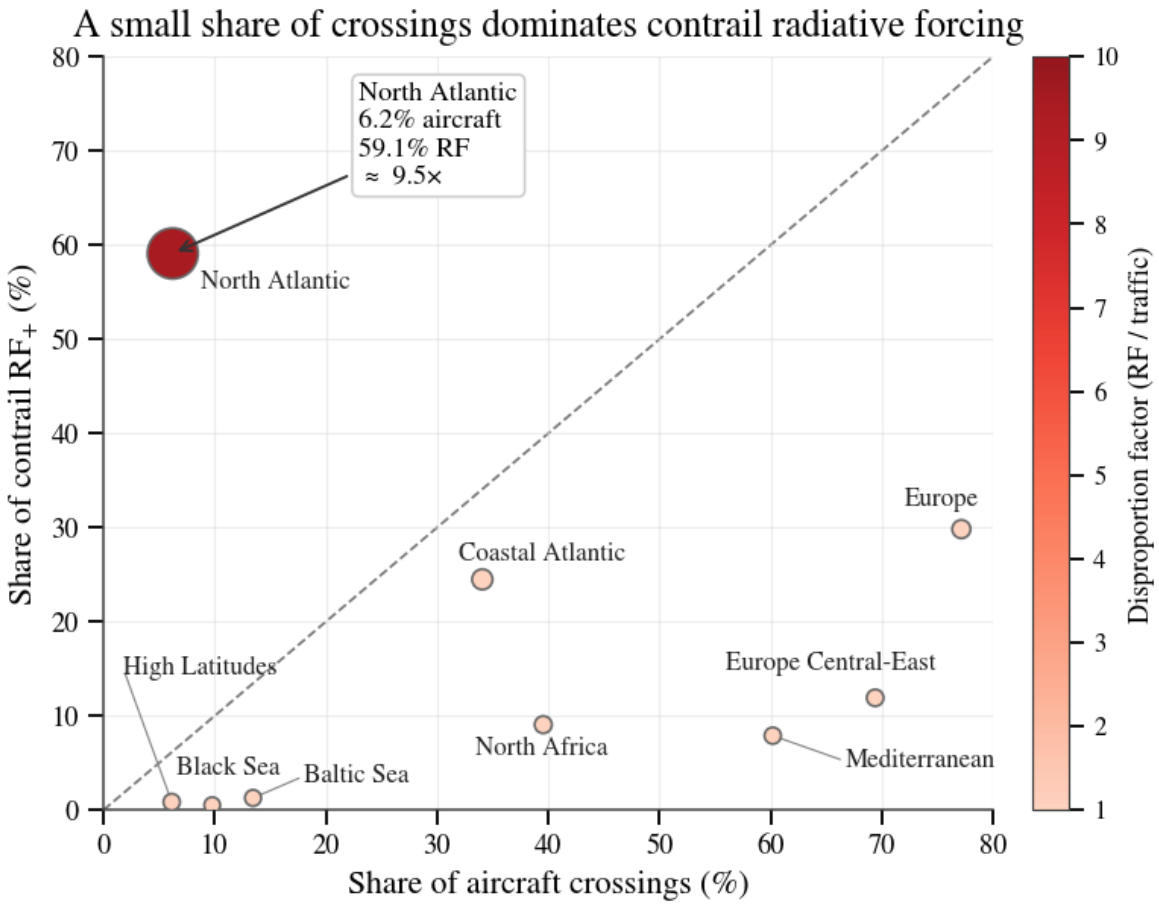

Figure 10: Contribution of specific regions to contrail radiative forcing (RF_+) relative to their share of air traffic. The dashed line denotes proportionality between traffic and forcing, while deviations from this line indicate regions with enhanced or reduced climate impact per unit traffic. Notably, the North Atlantic accounts for only ∼6% of crossings but contributes ∼59% of RF_+, corresponding to an ∼9.5-fold enhancement. Color shading represents the disproportion factor (RF/traffic), highlighting strong regional heterogeneity in contrail climate effects.